The Astrophysical Journal Letters, 978:L45 (12pp), 2025 January 10 https://doi.org/10.3847/2041-8213/ada158

Effective Resistivity in Relativistic Reconnection: A Prescription Based on Fully Kinetic Simulations

Abigail Moran[1], Lorenzo Sironi[1,2], Aviad Levis[3,4], Bart Ripperda[4,5,6,7], Elias R. Most[8,9], and Sebastiaan Selvi[1]
[1] Department of Astronomy, Columbia University, New York, NY 10027, USA; abigail.moran@columbia.edu
[2] Center for Computational Astrophysics, Flatiron Institute, 162 Fifth Ave., New York, NY 10010, USA
[3] Department of Computer Science, University of Toronto, Toronto, ON M5S 2E4, Canada
[4] David A. Dunlap Department of Astronomy & Astrophysics, University of Toronto, Toronto, ON M5S 3H4, Canada
[5] Canadian Institute for Theoretical Astrophysics, 60 St. George St., Toronto, ON M5S 3H8, Canada
[6] Department of Physics, University of Toronto, 60 St. George St., Toronto, ON M5S 1A7, Canada
[7] Perimeter Institute for Theoretical Physics, 31 Caroline St. North, Waterloo, ON N2L 2Y5, Canada
[8] TAPIR, Mailcode 350-17, California Institute of Technology, Pasadena, CA 91125, USA
[9] Walter Burke Institute for Theoretical Physics, California Institute of Technology, Pasadena, CA 91125, USA
Received 2024 November 29; revised 2024 December 18; accepted 2024 December 18; published 2025 January 10

Abstract

A variety of high-energy astrophysical phenomena are powered by the release—via magnetic reconnection—of the energy stored in oppositely directed fields. Single-fluid resistive magnetohydrodynamic (MHD) simulations with uniform resistivity yield dissipation rates that are much lower (by nearly 1 order of magnitude) than equivalent kinetic calculations. Reconnection-driven phenomena could be accordingly modeled in resistive MHD employing a nonuniform, "effective" resistivity informed by kinetic calculations. In this work, we analyze a suite of fully kinetic particle-in-cell (PIC) simulations of relativistic pair-plasma reconnection—where the magnetic energy is greater than the rest mass energy—for different strengths of the guide field orthogonal to the alternating component. We extract an empirical prescription for the effective resistivity, $\eta_{\rm eff} = \alpha B_0 |\boldsymbol{J}|^p / (|\boldsymbol{J}|^{p+1} + (en_t c)^{p+1})$, where B_0 is the reconnecting magnetic field strength, $\boldsymbol{J}$ is the current density, n_t is the lab-frame total number density, e is the elementary charge, and c is the speed of light. The guide field dependence is encoded in α and p, which we fit to PIC data. This resistivity formulation—which relies only on single-fluid MHD quantities—successfully reproduces the spatial structure and strength of nonideal electric fields and thus provides a promising strategy for enhancing the reconnection rate in resistive MHD simulations.

Unified Astronomy Thesaurus concepts: High energy astrophysics (739); Plasma astrophysics (1261); Magnetic fields (994); Magnetohydrodynamics (1964)

1. Introduction

Strong magnetic fields in astrophysical compact sources provide a reservoir of magnetic energy. This energy can be released to the plasma—resulting in particle acceleration and nonthermal emission—when anti-aligned field lines annihilate in a process called magnetic reconnection. In a number of astrophysical sources, reconnection occurs in the relativistic regime, where the magnetic energy exceeds the plasma rest mass energy (for reviews, see M. Hoshino & Y. Lyubarsky 2012; D. Kagan et al. 2015; F. Guo et al. 2020, 2024). Relativistic reconnection can power a variety of high-energy phenomena, such as emission from black hole coronae, magnetar flares, blazar jet flares, radio and gamma-ray emission from pulsar magnetospheres, fast radio bursts, and flares from supermassive black hole magnetospheres.

Magnetic reconnection refers to the breaking and reconnecting of oppositely directed field lines. This requires the "ideal" condition

$$\boldsymbol{E} + \frac{\langle \boldsymbol{v}_s \rangle}{c} \times \boldsymbol{B} = 0$$

to be violated for each relevant plasma species s. Here, $\boldsymbol{E}$ and $\boldsymbol{B}$ are the electromagnetic fields, while $\langle \boldsymbol{v}_s \rangle$ is the mean three-velocity of species s. In *collisional* plasmas, the ideal condition can be broken by resistive effects due to binary particle collisions—encoded by the resistivity appearing in Ohm's law. When resistive effects are not important, the magnetic field is "frozen" into the fluid, as prescribed by Alfvén's theorem (H. Alfvén 1943; also known as the flux freezing theorem). In dilute astrophysical plasmas, binary collisions are rare, so the collisional resistivity is often insufficient to break flux freezing on interesting time and length scales.

Reconnection occurring in the *collisionless* regime requires a kinetic description. Since the typical separation between plasma scales and global scales is very large, kinetic descriptions, e.g., employing the particle-in-cell (PIC) method, are unaffordable at realistic scale separations. Fluid-type approaches such as magnetohydrodynamics (MHD), while suitable to model the global dynamics, are by construction collisional and therefore unable to capture collisionless effects. In fact, single-fluid resistive MHD simulations with uniform resistivity yield reconnection rates in the plasmoid-dominated regime that are much lower (by nearly 1 order of magnitude) than equivalent kinetic calculations (J. Birn et al. 2001; D. A. Uzdensky et al. 2010; L. Comisso & A. Bhattacharjee 2016; P. A. Cassak et al. 2017). This discrepancy impacts the timescale of reconnection-powered flares, e.g., in black hole magnetospheres (A. Bransgrove et al. 2021; A. Galishnikova et al. 2023).

A large body of work has focused on identifying the processes that can break the ideal condition in collisionless or weakly collisional plasmas—here, wave–particle interactions provide a form of effective collisionality. In pair plasmas, fast reconnection is mediated by the off-diagonal terms of the pressure tensor (N. Bessho & A. Bhattacharjee 2005, 2007; M. Hesse & S. Zenitani 2007; M. Melzani et al. 2014; M. Goodbred & Y.-H. Liu 2022), which are also important for electron-ion plasmas in the small, electron-scale diffusion region (L. R. Lyons & D. C. Pridmore-Brown 1990; R. Horiuchi & T. Sato 1994; H. J. Cai & L. C. Lee 1997; M. M. Kuznetsova et al. 1998; J. Egedal et al. 2019).

By identifying the dominant contributors to the breaking of flux freezing in collisionless plasmas, it may be possible to write the corresponding nonideal electric field as $\eta_{\rm eff}\boldsymbol{J}$—here, $\eta_{\rm eff}$ is some effective resistivity and $\boldsymbol{J}$ the electric current density—which could be incorporated in resistive, single-fluid MHD approaches as a kinetically motivated subgrid prescription (R. M. Kulsrud 1998, 2001; D. Biskamp & E. Schwarz 2001; D. Uzdensky 2003; N. Bessho & A. Bhattacharjee 2010; S. Zenitani et al. 2010; B. Ripperda et al. 2019; N. F. Loureiro 2023). In general, parameterizing kinetic effects as an effective resistivity is a nontrivial task (e.g., E. Hirvijoki et al. 2016; M. Lingam et al. 2017). By means of a statistical analysis based on PIC simulations, S. Selvi et al. (2023) identified the mechanisms driving the nonideal electric field in the generalized Ohm's law, for the case of relativistic pair-plasma reconnection. The effective resistivity proposed by S. Selvi et al. (2023) for the zero guide field case (and earlier suggested by N. Bessho & A. Bhattacharjee 2007, 2012) has been shown to successfully enhance the reconnection rate in resistive MHD simulations (M. Bugli et al. 2024).

As we discuss below, the form of effective resistivity proposed by S. Selvi et al. (2023) suffers from a few limitations, which may hamper its applicability. In this work, rather than analyzing nonideal terms in the generalized Ohm's law, we adopt an empirical approach. We perform a suite of PIC simulations of relativistic pair-plasma reconnection with varying guide field strength, and we formulate an empirical prescription for the effective resistivity $\eta_{\rm eff}$, which is derived directly from our PIC runs through a data-driven parameterization. Our proposed model depends only on the electric current density and the plasma number density, both of which are readily available in resistive MHD codes. As compared to S. Selvi et al. (2023), the form of $\eta_{\rm eff}$ that we obtain has four main advantages: it is written explicitly in single-fluid MHD quantities, does not depend on spatial derivatives, is coordinate agnostic, and is valid for any guide field. We demonstrate that the formulation of $\eta_{\rm eff}$ we propose successfully reproduces the spatial structure and strength of nonideal electric fields in our PIC simulations, thus providing a promising strategy for enhancing the reconnection rate in resistive MHD approaches.

2. PIC Simulation Setup

Our simulations are performed with the 3D PIC code TRISTAN-MP (A. Spitkovsky 2005). We use a 2D $x-y$ domain, but we track all components of the particle velocity and of the electromagnetic fields. Although the physics of particle acceleration in relativistic reconnection is dramatically different between 2D and 3D (H. Zhang et al. 2021, 2023), the reconnection rate—which is defined as the plasma inflow velocity and is the focus of our work—is roughly the same (e.g., L. Sironi & A. Spitkovsky 2014; G. R. Werner & D. A. Uzdensky 2017).

The in-plane magnetic field is initialized in a "Harris equilibrium" (E. G. Harris 1962), $\boldsymbol{B}_{\rm in} = B_0\hat{\boldsymbol{x}}\tanh(2\pi y/\Delta)$, where the direction of the in-plane field reverses at $y = 0$ over a thickness $\Delta = 70\,c/\omega_p$. Here, c/ω_p is the depth of the plasma skin, and $\omega_p = \sqrt{4\pi n_0 e^2/m}$ is the plasma frequency, where n_0 is the total number density of electron–positron pairs far from the layer, m is the electron/positron mass, and e is the elementary charge. We parameterize the field strength in the plane B_0 by the magnetization

$$\sigma = \frac{B_0^2}{4\pi n_0 mc^2},$$

which we take to be $\sigma = 50$. We consider guide fields of magnitude $B_g/B_0 = 0.0$, 0.3, 0.6, and 1.0.

The upstream region is initialized with $n_0 = 64$ particles per cell (including both species). We resolve the plasma skin depth c/ω_p with five cells and evolve the simulation up to $4500\,\omega_p^{-1}$. In Appendix A, we choose $c/\omega_p = 20$ cells and demonstrate that our results are robust to spatial resolution. In Appendix A, we also display cases that include strong synchrotron cooling losses. For our fiducial runs, the length of the domain in the x-direction of plasma outflows is $L_x = 1920c/\omega_p$. We use open boundaries for fields and particles along the x-direction. The box grows in the y-direction as the simulation progresses, allowing for more plasma and magnetic flux to enter the domain. At the end of the simulations, the length of our box along the y-axis is comparable to L_x.

3. Resistivity Formulation

We begin by considering Ohm's law for resistive relativistic single-fluid MHD (S. S. Komissarov 2007):

$$\Gamma\left[\boldsymbol{E} + \frac{\boldsymbol{v}}{c}\times\boldsymbol{B} - \frac{1}{c^2}(\boldsymbol{E}\cdot\boldsymbol{v})\boldsymbol{v}\right] = \eta(\boldsymbol{J} - \rho_e\boldsymbol{v}), \tag{1}$$

where Γ is the bulk fluid Lorentz factor, $\boldsymbol{v}$ is the fluid three-velocity, ρ_e is the electric charge density, and η is the collisional resistivity. In a collisionless plasma, the replacement of η by $\eta_{\rm eff}$ in Equation (1) can be regarded as the definition of an effective resistivity that incorporates kinetic effects in single-fluid resistive MHD. As we justify in Appendix B, we can further assume that $|\rho_e\boldsymbol{v}| \ll |\boldsymbol{J}|$ and $\Gamma \simeq 1$ and that the third term in the square bracket is negligible, which yields

$$\boldsymbol{E}^* \equiv \boldsymbol{E} + \frac{\boldsymbol{v}}{c}\times\boldsymbol{B} = \eta_{\rm eff}\boldsymbol{J}, \tag{2}$$

where $\boldsymbol{E}^*$ is the nonideal electric field. The spatial structure of the z-component of the nonideal electric field, E_z^*, is shown in the bottom row of Figure 1, at a representative time after the simulation has achieved a quasi-steady state (i.e., the reconnection rate attains a quasi-steady value). The figure emphasizes that nonideal regions are generally larger for increasing guide field. We also present the spatial structure of the total particle density n_t (top row; in units of n_0) and of the magnetic energy density (middle row; in units of $B_0^2/8\pi$), for both $B_g/B_0 = 0$ (left column) and $B_g/B_0 = 1$ (right column).

In order to determine the effective resistivity $\eta_{\rm eff}$, we focus on the z-component of Equation (2), which dominates the nonideal field for the whole range of B_g/B_0 we explore. The

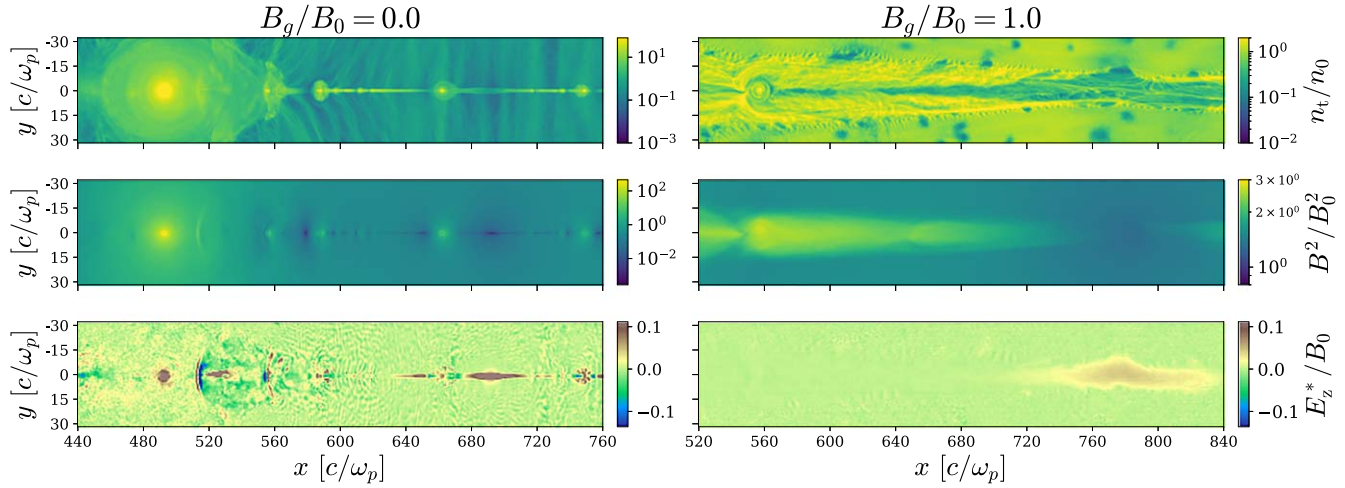

Figure 1. Spatial distribution of the particle number density n_t (top row; in units of n_0) of the magnetic energy density (middle row; in units of $B_0^2/8\pi$) and of the z-component of the nonideal electric field as defined in Equation (2) (bottom row; in units of B_0), for simulations with $B_g/B_0 = 0$ (left) and $B_g/B_0 = 1$ (right). The snapshots are taken at a representative time to show the nonideal electric field and plasmoid structure after the simulations have achieved a quasi-steady state. We define $x = 0$ as the edge of the simulation domain (so, the plot only shows a portion of the domain), while $y = 0$ in the midplane.

z-component E_z^* is the only significant component for zero guide field, being 1 to 2 orders of magnitude larger than other components; for nonzero guide fields, we still determine $\eta_{\rm eff}$ from $E_z^* = \eta_{\rm eff} J_z$, but we show that the same effective resistivity properly describes other components, specifically $E_x^* = \eta_{\rm eff} J_x$ (see Section 4). Our new prescription for the effective resistivity is derived using a data-driven phenomenological model with two free parameters, which are benchmarked with PIC simulations. We compare the performance of our prescription to the resistivity model from S. Selvi et al. (2023)—based on a kinetic approach—and to its extension employing MHD quantities.

3.1. Kinetically Motivated Resistivity

S. Selvi et al. (2023) analyzed PIC simulations of relativistic reconnection in pair plasmas and identified the terms that dominate the nonideal electric field in the generalized Ohm's law (M. Hesse & S. Zenitani 2007). Their analysis was restricted to regions of electric dominance, defined as having $E_z^2 > B_x^2 + B_y^2$ (which is nearly identical to the condition $|\boldsymbol{E}| > |\boldsymbol{B}|$ in the case of zero guide field). They found that the z-component of the nonideal electric field could be written as

$$E_z^* = \eta_{S23,\rm kin} J_z = \left[\frac{m}{n_t e^2}\frac{\langle u_{ez}\rangle}{\langle v_{ez}\rangle}\partial_y\langle v_{ey}\rangle\right] J_z, \tag{3}$$

where n_t is the total number density (including both electrons and positrons); $\langle v_{ez}\rangle$ and $\langle u_{ez}\rangle$ are, respectively, the mean electron three- and four-velocity in the z-direction;[10] and $\langle v_{ey}\rangle \simeq v_y$ is the mean three-velocity along y, which is roughly the same for both species (hereafter, we call v_y the single-fluid y velocity).

The effective resistivity proposed by S. Selvi et al. (2023) in Equation (3) has a few limitations: (i) it provides a satisfactory description of the nonideal electric field only for $B_g = 0$; and (ii) it was derived considering regions of electric dominance, which are only a subset of the regions hosting nonideal fields (L. Sironi 2022; S. R. Totorica et al. 2023), where resistive effects are important. In order to derive Equation (3), S. Selvi et al. (2023) used the approximation

$$\partial_y(n_e\langle v_{ey}\rangle\langle u_{ez}\rangle) \approx n_e\langle u_{ez}\rangle\partial_y\langle v_{ey}\rangle, \tag{4}$$

which is valid only in the vicinity of the center of the current sheet. In fact, as shown in Figure 2, the effective resistivity in Equation (3) (hereafter, $\eta_{S23,\rm kin}$) provides a reasonable description of the nonideal field near the center of the layer ($|y|\omega_p/c \lesssim 1$), where $|\boldsymbol{E}| > |\boldsymbol{B}|$ (blue shaded area), but it significantly overestimates the ground truth (i.e., the direct measurement of E_z^* from PIC runs) farther away from the layer ($|y|\omega_p/c \gtrsim 1$).

For use in single-fluid MHD codes, Equation (3) needs to be rewritten using fluid quantities. As we have already discussed above, the mean three-velocity along y is roughly the same for the two species, $\langle v_{ey}\rangle \simeq \langle v_y\rangle$. The most reasonable approximation for the ratio between the mean four- and three-velocities of a given species is $\langle u_{ez}\rangle/\langle v_{ez}\rangle \simeq \langle\gamma\rangle$, where the mean particle Lorentz factor (including both bulk and internal motions) can be derived from the T^{00} component of the stress energy tensor as $\langle\gamma\rangle = T^{00}/n_t mc^2$. This leads to a form of Equation (3) that can be implemented in MHD:

$$E_z^* = \eta_{S23,\rm MHD} J_z = \left[\frac{m}{n_t e^2}\langle\gamma\rangle \quad \partial_y v_y\right] J_z. \tag{5}$$

As shown in Figure 3, Equation (5) is an excellent approximation of the kinetic form in Equation (3) (compare top right and bottom right panels). However, as anticipated in Figure 2, the two forms overestimate the true resistivity (top left of Figure 3), especially at the boundaries of the current layer. In an earlier version of S. Selvi et al. (2023), Equation (3) was cast in an alternative form, approximating

$$\frac{\langle u_{ez}\rangle}{\langle v_{ez}\rangle} \simeq \frac{1}{\sqrt{1 - (J_z/en_t c)^2}}, \tag{6}$$

which only holds if each species has negligible internal motions and moves in the z-direction with dimensionless drift

[10] At X-points, positrons and electrons have opposite $\langle v_{ez}\rangle$ and $\langle u_{ez}\rangle$, but the ratio $\langle u_{ez}\rangle/\langle v_{ez}\rangle$ is the same for both species.

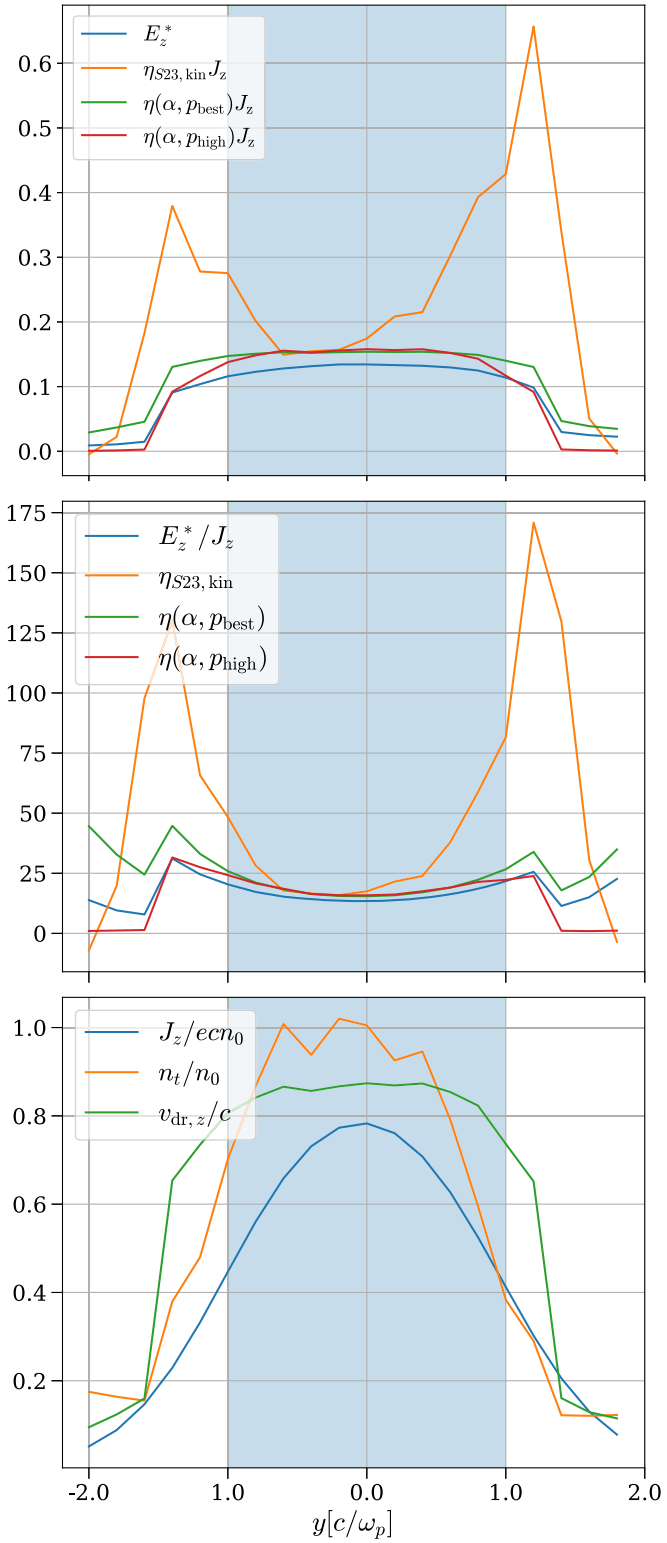

Figure 2. 1D slice of the domain along y through an X-point, for the simulation with zero guide field. The top panel shows the z-component of the nonideal electric field in units of B_0; the middle panel shows the resistivity; and the bottom panel shows the electric current J_z (in blue), the number density n_t (in orange), and the drift speed $v_{dr,z}/c \simeq J_z/en_tc$ (in green). In the top and middle panels, we present in blue the ground truth obtained directly from our simulation, while other colors show various choices for η_{eff}, as described in the legend. Our prescription for resistivity (Equation (10)) is shown as $\eta(\alpha, p_{\mathrm{best}})$ and $\eta(\alpha, p_{\mathrm{high}})$ for the values of p defined in Section 4 and corresponding α values. Regions where $|\boldsymbol{E}| > |\boldsymbol{B}|$ are shaded in blue.

speed of $|J_z|/en_tc$. This was recently rewritten by M. Bugli et al. (2024) in the form

$$\eta_{B24} = \frac{1}{en_tc}\sqrt{\left(\frac{mc}{e}\partial_y v_y\right)^2 + (\Gamma E_z^*)^2}\,. \tag{7}$$

While the approximation in Equation (6) leading to Equation (7) does not generally hold, as shown by the poor agreement between the top right and bottom left panels in Figure 3, Equation (7) appears to provide a remarkably good proxy for the ground truth (compare top left and bottom left). While Equation (7) appears to improve upon the kinetically motivated model by S. Selvi et al. (2023), it loses some of the physical motivation of Equations (3) and (5).

While useful, the forms of effective resistivity presented in this subsection have some undesirable properties: (i) they only apply to the case of zero guide field; (ii) they contain a spatial derivative, which makes them difficult to include in relativistic MHD codes while maintaining causality (L. Del Zanna et al. 2007); (iii) they only apply to the main layer and not to the antireconnection layers in between merging plasmoids (which extend along y and for which the relevant velocity derivative is $\partial_x v_x$); and (iv) they retain a dependence on the system geometry (e.g., via the z-component E_z^*), which makes it hard to incorporate in global MHD simulations where current sheets will be curved, oscillating, and generally not aligned with the coordinate axes. In the Section 3.2, we turn to a more agnostic approach that avoids some of these issues.

3.2. Prescriptive Resistivity

To overcome the limitations of the model by S. Selvi et al. (2023), we propose an empirical approach. We expect that in regions of strong currents—as defined below—the nonideal electric field should approach $|\boldsymbol{E}^*| \to (v_{\mathrm{in}}/c)B_0$, where v_{in} is the reconnection rate (i.e., the inflow velocity of plasma into the layer; see Figure 4), which implies that the effective resistivity should be

$$\eta_{\mathrm{eff}} \to \frac{v_{\mathrm{in}}}{c}\frac{B_0}{|\boldsymbol{J}|}. \tag{8}$$

A choice of $\eta_{\mathrm{eff}} \propto |\boldsymbol{J}|^{-1}$ is inapplicable in regions of small electric currents, where the resistivity should vanish. We therefore design a form such that $\eta_{\mathrm{eff}} \propto |\boldsymbol{J}|^p$ for small current densities, where $p > 0$ is a free parameter. More precisely, this should occur where $|\boldsymbol{J}| \ll en_tc$. Adding a normalization factor α, this motivates choosing a form

$$\eta_{\mathrm{eff}} = \frac{\alpha B_0 |\boldsymbol{J}|^p}{|\boldsymbol{J}|^{p+1} + (en_tc)^{p+1}} = \frac{\alpha B_0}{|\boldsymbol{J}|[1 + (en_tc/|\boldsymbol{J}|)^{p+1}]}. \tag{9}$$

We will determine free parameters α and p from PIC simulations. This scales as $\eta_{\mathrm{eff}} \propto |\boldsymbol{J}|^p/(en_tc)^{p+1}$ at small currents and approaches $\eta_{\mathrm{eff}} = \alpha B_0/(2|\boldsymbol{J}|)$ for $|\boldsymbol{J}| \simeq en_tc$. We therefore expect $\alpha/2 \simeq v_{\mathrm{in}}/c$, as we indeed find below (see also Figure 4). The condition $|\boldsymbol{J}| \simeq en_tc$ corresponds to the charge starvation regime, i.e., all charge carriers move at near the speed of light. This limit is indeed realized in the inner region of the current sheet: as the bottom panel of Figure 2 shows, the 1D profiles of J_z and n_t have the same shape, suggesting a

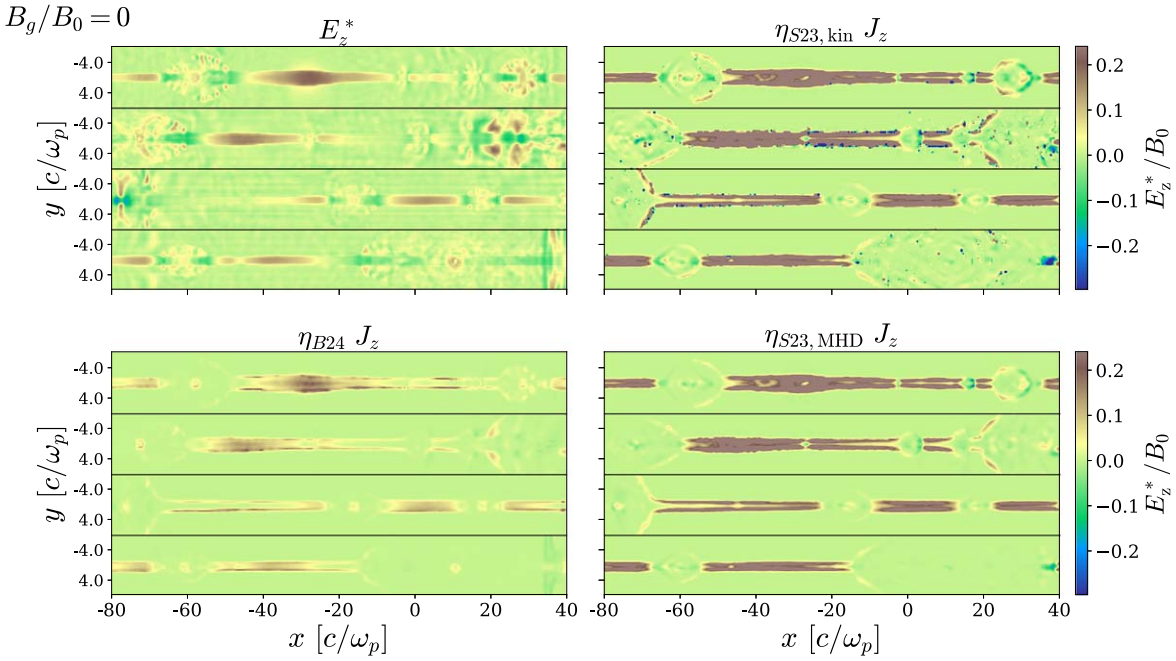

Figure 3. A comparison between the measured nonideal electric field E_z^* (top left) and its reconstruction $\eta_{\mathrm{eff}}J_z$ based on different choices of η_{eff}: $\eta_{\mathrm{S23,kin}}$ (Equation (3)) in top right, η_{B24} (Equation (7)) in bottom left, and $\eta_{\mathrm{S23,MHD}}$ (Equation (5)) in bottom right. All panels are normalized to B_0. Within each panel, horizontal black lines separate different time snapshots: the first one is taken when the reconnection rate shown in Figure 4 first settles into a steady state, and the others follow after 450, 810, and 1080 ω_p^{-1}, respectively. The horizontal axis is measured with respect to the center of the portion of domain that is displayed. The derivatives in Equations (3), (5), and (7) are computed as numerical derivatives on cells downsampled by a factor of 2.

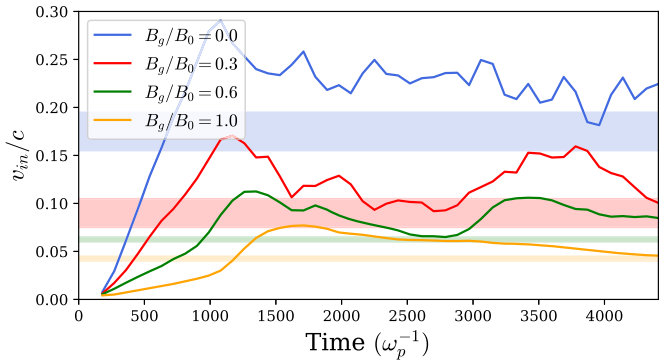

Figure 4. Reconnection rate (i.e., the plasma inflow velocity normalized by c) over time for each guide field case, as indicated in the legend. The reconnection rate is measured as the mean inflow velocity in the region $y = [-672, 672]c/\omega_p$. In the same color, we show with the shaded area the acceptable ranges of $\alpha/2$ of our resistivity prescription, which we define in Section 3.2.

nearly constant drift velocity $J_z/en_t \simeq 0.9\,c$. In fact, if we define the drift velocity $\boldsymbol{v}_{dr} \equiv \boldsymbol{J}/en_t$, our prescription can be written as

$$\eta_{\mathrm{eff}} = \frac{\alpha B_0}{|\boldsymbol{J}|[1 + (c/|\boldsymbol{v}_{dr}|)^{p+1}]}. \tag{10}$$

In the inner region of the current sheet, where $|\boldsymbol{v}_{dr}| \simeq c$ (green line in the bottom panel of Figure 2), we obtain $\eta_{\mathrm{eff}} \propto |\boldsymbol{J}|^{-1}$, which matches the double-peaked shape of the ground truth (i.e., E_z/J_z) in the middle panel of Figure 2. We emphasize that the density dependence in $\boldsymbol{v}_{dr} \propto \boldsymbol{J}/n_t$ is a key ingredient of our resistivity model—in fact, the density in the middle of the sheet can be significantly larger than in the immediate upstream; see bottom panel of Figure 2.

In Section 5, we provide an equivalent, more general version of Equation (9) suitable for implementation within resistive MHD codes.

4. Results

To determine the optimal values of α and p in Equation (10), we consider the z-component of the nonideal field and define a loss, or data-fit metric

$$L(\alpha, p) = \sum_{x,y} |E_z^* - \eta_{\mathrm{eff}}(\alpha, p) J_z|^2 |E_z^*|, \tag{11}$$

i.e., we minimize the L2 loss (the mean squared error) between $\eta_{\mathrm{eff}}J_z$ and the measured E_z^*. The loss is weighted by $|E_z^*|$ to ensure that the large regions with negligible nonideal fields do not skew our findings. We calculate the optimal parameters α and p by minimizing this loss through a simple grid search. We create a composite domain including several time snapshots of the PIC simulations. For each case with varying guide field, the snapshots (roughly 15 in each case) are equally spaced from the time when reconnection first attains a quasi-steady state up to the end of our simulations, $\omega_p t = 4500$. For each snapshot, we consider a region extending along the whole domain in x and with thickness $64\,c/\omega_p$ along y (sufficient to enclose the largest plasmoids), centered around the current sheet. As a representative case, the loss for $B_g/B_0 = 1$ is shown in Figure 5. The manifold shows that a valley of small loss, with values of L near the global minimum (shown by the red point), stretches across a wide range of p.

In order to determine the optimal p and define a range of acceptable values, we adopt the following procedure. We begin by minimizing the loss on many small, randomly selected regions (hereafter, "patches") of the composite domain. In each

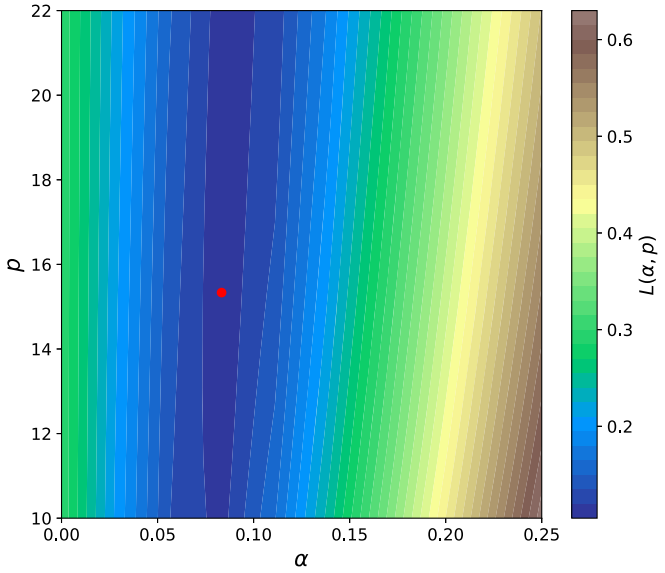

Figure 5. Loss manifold computed with Equation (11) for $B_g/B_0 = 1$, as a function of α and p. The red point marks the (α, p) combination of minimum loss. Many combinations in the dark blue valley produce losses very close to the global minimum. A correlation between the two parameters can also be seen.

Table 1
Best-fit p with Upper and Lower Limits of the Acceptable Range (Last Column) for Each Guide Field

B_g/B_0	Patch Dim. (c/ω_p)	Num. Patches	p
0.0	[80, 16]	2500	$0.00^{+1.73}_{-0.00}$
0.3	[160, 40]	2000	$9.59^{+8.59}_{-5.37}$
0.6	[240, 40]	600	$15.4^{+3.8}_{-2.1}$
1.0	[120, 24]	1500	$18.2^{+5.1}_{-6.2}$

Note. We indicate the dimensions (along x and y, respectively) of the patches used to compute the distribution of values of p (second column) as well as the number of patches (third column).

Table 2
For Each Guide Field We Show the Best-fit Value of p (Second Column) and the Lowest and Highest Acceptable Values (Third Column)

B_g/B_0	$p_{\rm best}$	$[p_{\rm low}, p_{\rm high}]$	$\alpha(p)$
0.0	0.00	[0.00, 1.73]	$0.0369\,p + 0.3268$
0.3	9.59	[4.22, 18.2]	$0.0046\,p + 0.1295$
0.6	15.4	[13.3, 19.2]	$0.0017\,p + 0.1002$
1.0	18.2	[12.0, 23.3]	$0.0010\,p + 0.0702$

Note. These bounds are calculated as described in the text. We also show a function that returns the optimal α for a given p within this range (fourth column).

small patch, we find that there is a clearly preferred value of p (i.e., a sharp minimum of Equation (11), as opposed to the wide minimum we find on global scales), which we will use to define a range of acceptable values of p. We continue adding regions until the results converge, meaning that repeatedly selecting the same number of random patches produces the same outcome, regardless of which regions are chosen. We vary the patch size depending on the guide field strength, such that the patch is twice larger than the typical extent of a region with significant nonideal fields (see bottom panels in Figure 1). The number of

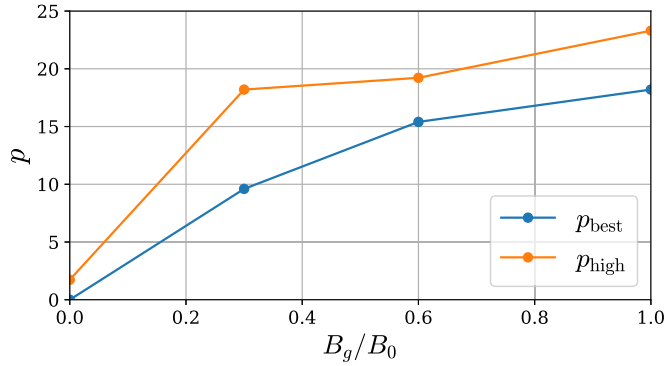

Figure 6. Best fit ($p_{\rm best}$) and upper bound ($p_{\rm high}$) as a function of guide field strength.

Table 3
The Results Obtained When Varying the Size of Patches Used to Compute p (Default Values Are in Table 1) and the Percentiles Used in the Threshold for Patch Selection (Default Values Are 55–45)

B_g/B_0	Patch Dim. (c/ω_p)	Threshold per.	p
0.0	[60, 32]	55–45	$0.00^{+1.26}_{-0.00}$
0.0	[80, 16]	60–40	$0.00^{+1.33}_{-0.00}$
1.0	[80, 40]	55–45	$17.8^{+5.4}_{-5.9}$
1.0	[120, 24]	60–40	$18.2^{+4.8}_{-4.8}$

Note. As before, for $B_g/B_0 = 0.0$, we use 2500 patches, and for $B_g/B_0 = 1.0$, we use 1500 patches.

Table 4
Performance L2 Loss of Various Resistivity Models as Compared to the Measured E_z^*, for Different Guide Fields

B_g/B_0	Model	$\lvert E_z^*\rvert$	$(E_z^*)^2$	1
0.0	$\eta(\alpha, p_{\rm best})J_z$	5.052	3.517	21.35
	$\eta(\alpha, p_{\rm high})J_z$	5.157	3.599	17.93
0.3	$\eta(\alpha, p_{\rm best})J_z$	3.121	1.085	12.97
	$\eta(\alpha, p_{\rm high})J_z$	3.129	1.086	13.00
0.6	$\eta(\alpha, p_{\rm best})J_z$	0.410	0.067	3.913
	$\eta(\alpha, p_{\rm high})J_z$	0.412	0.067	3.920
1.0	$\eta(\alpha, p_{\rm best})J_z$	0.108	0.008	2.047
	$\eta(\alpha, p_{\rm high})J_z$	0.110	0.009	2.048

Note. We vary the weight of the loss function as indicated in the last three columns. We exclude cells where $n_t < 1$.

patches and the patch size used in this step are indicated in Table 1. To ensure that the loss in a given patch is informative (which is not the case for patches with small E_z^*), we require

$$\text{median}(E_z^*)_{\rm patch} > \text{median}(E_z^*)_{\rm global} + \text{threshold}, \quad (12)$$

where the median is computed in a given patch (left-hand side) or over the whole composite domain (right-hand side). The threshold indicated on the right-hand side is the difference between the 55th and 45th percentiles of the distribution of E_z^* in the whole domain. We use these percentiles instead of the standard interquartile range to ensure a more robust analysis that includes a greater portion of the domain. We define $p_{\rm best}$ as the value that minimizes the loss when considering the combined area of all patches.

We then create the distribution of values of p that minimize the loss in each patch. The difference $\Delta p_{\rm low}$ between the 50th

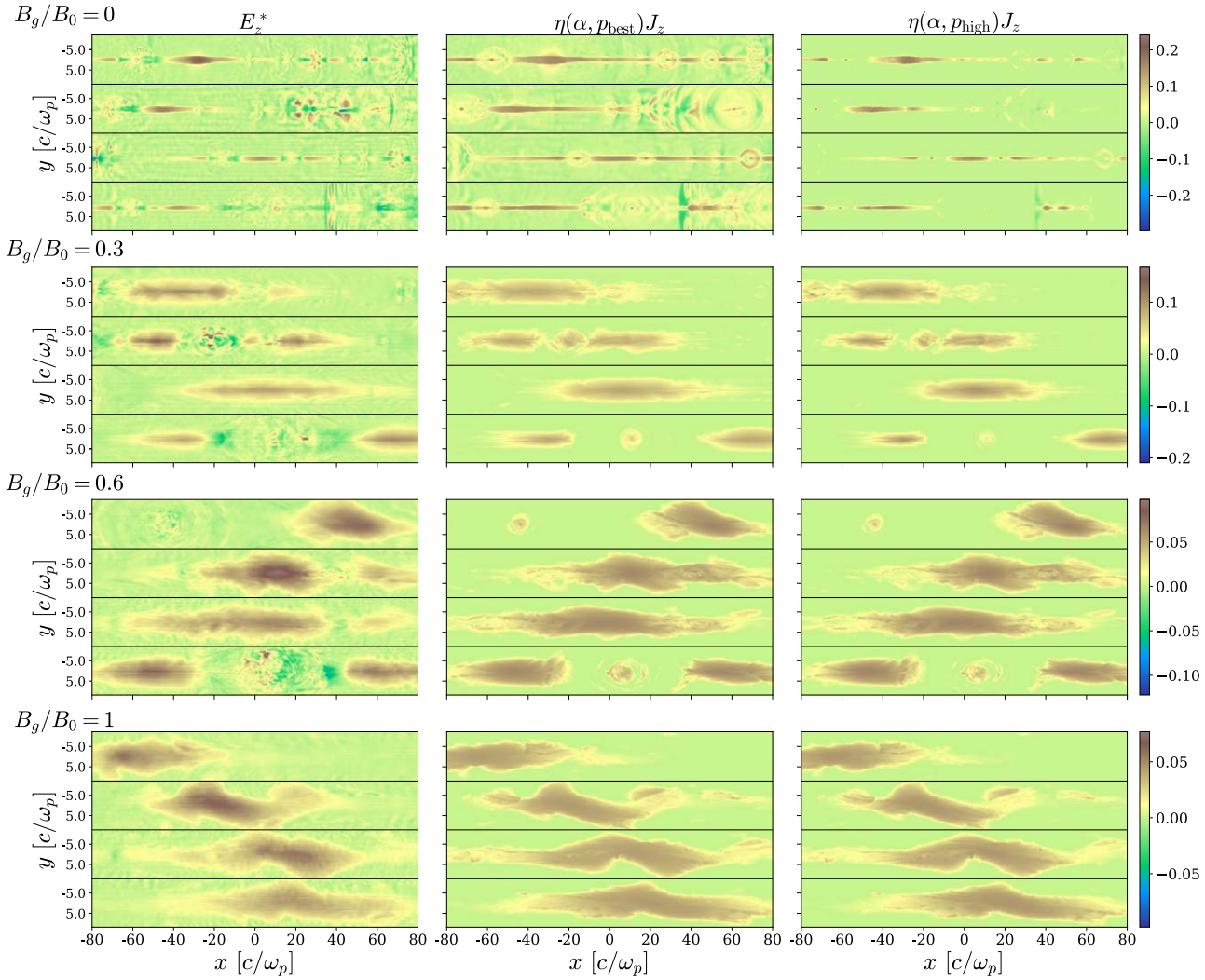

Figure 7. A comparison between the measured nonideal electric field E_z^* (left column) and its reconstruction $\eta_{\rm eff}J_z$ based on our prescription in Equation (10), for the whole range of guide fields we explored. The middle column shows $\eta_{\rm eff}(\alpha, p_{\rm best})J_z$ (here, α is the value corresponding to $p_{\rm best}$ based on the linear fit in Table 2), while the right column shows $\eta_{\rm eff}(\alpha, p_{\rm high})J_z$ (α is the value corresponding to $p_{\rm high}$). All panels are normalized to B_0. Within each panel, horizontal black lines separate different time snapshots: the first one is taken when the reconnection rate shown in Figure 4 first settles into a steady state, and the others follow after 450, 810, and 1080 ω_p^{-1} respectively. The horizontal axis is measured with respect to the center of the portion of domain that is displayed (which is a small fraction of the composite domain used to determine the best-fit values of α and p).

and 16th percentiles of this distribution gives the lower limit on allowed values of p, $p_{\rm low} = \max[p_{\rm best} - \Delta p_{\rm low}, 0]$, while the difference $\Delta p_{\rm high}$ between the 84th and 50th percentiles gives the upper limit $p_{\rm high} = p_{\rm best} + \Delta p_{\rm high}$. These values are indicated for each guide field in Table 2. We plot $p_{\rm best}$ and $p_{\rm high}$ as a function of guide field in Figure 6. Table 3 demonstrates that our findings do not depend much on the patch size or the threshold percentiles employed in Equation (12). We find that the optimal value of p is robust to patch size and varies by $\lesssim$2% when the threshold percentiles are altered. Similarly, the upper and lower limits on on p decrease by a modest amount when varying these parameters.

Within the range $[p_{\rm low}, p_{\rm high}]$, we then consider 15 evenly spaced values of p. For each value, we find the optimal α using the loss function on the combined area of all patches. This reveals that the two parameters are correlated. We interpolate to find $\alpha(p)$ and show the resulting linear fits in Table 2. The range of $\alpha/2$ corresponding to the interval $[p_{\rm low}, p_{\rm high}]$ is shown by the colored shaded bands in Figure 4. As expected, $\alpha/2$ matches well with the measured reconnection rate, for all guide field cases (solid lines of the same color).

We finally assess how well the reconstructed $\eta_{\rm eff}J_z$ captures the nonideal field E_z^* obtained directly from our PIC simulations. Table 4 shows the L2 loss obtained for $p = p_{\rm best}$ or $p = p_{\rm high}$. For each of the two choices, the corresponding value of α is obtained from the linear fit in Table 2. We find that, regardless of the weight adopted in the loss function (no weight, $|E_z^*|$ or $(E_z^*)^2$), the L2 loss increases by less than ~10% when using $p_{\rm high}$, as compared to choosing $p_{\rm best}$ (and for the unweighted loss of $B_g/B_0 = 0$, $p_{\rm high}$ performs better than $p_{\rm best}$). We therefore regard all solutions within the range of $[p_{\rm best}, p_{\rm high}]$ as acceptable.

This is also confirmed by the 2D spatial profiles shown in Figure 7. For all the guide fields we explore, we present the ground truth in the left column (i.e., the nonideal field E_z^* measured directly from our simulations), the reconstruction $\eta_{\rm eff}(\alpha, p_{\rm best})J_z$ in the middle column (here, α is the value corresponding to $p_{\rm best}$ based on the linear fit in Table 2), and the reconstruction $\eta_{\rm eff}(\alpha, p_{\rm high})J_z$ in the right column (here, α is

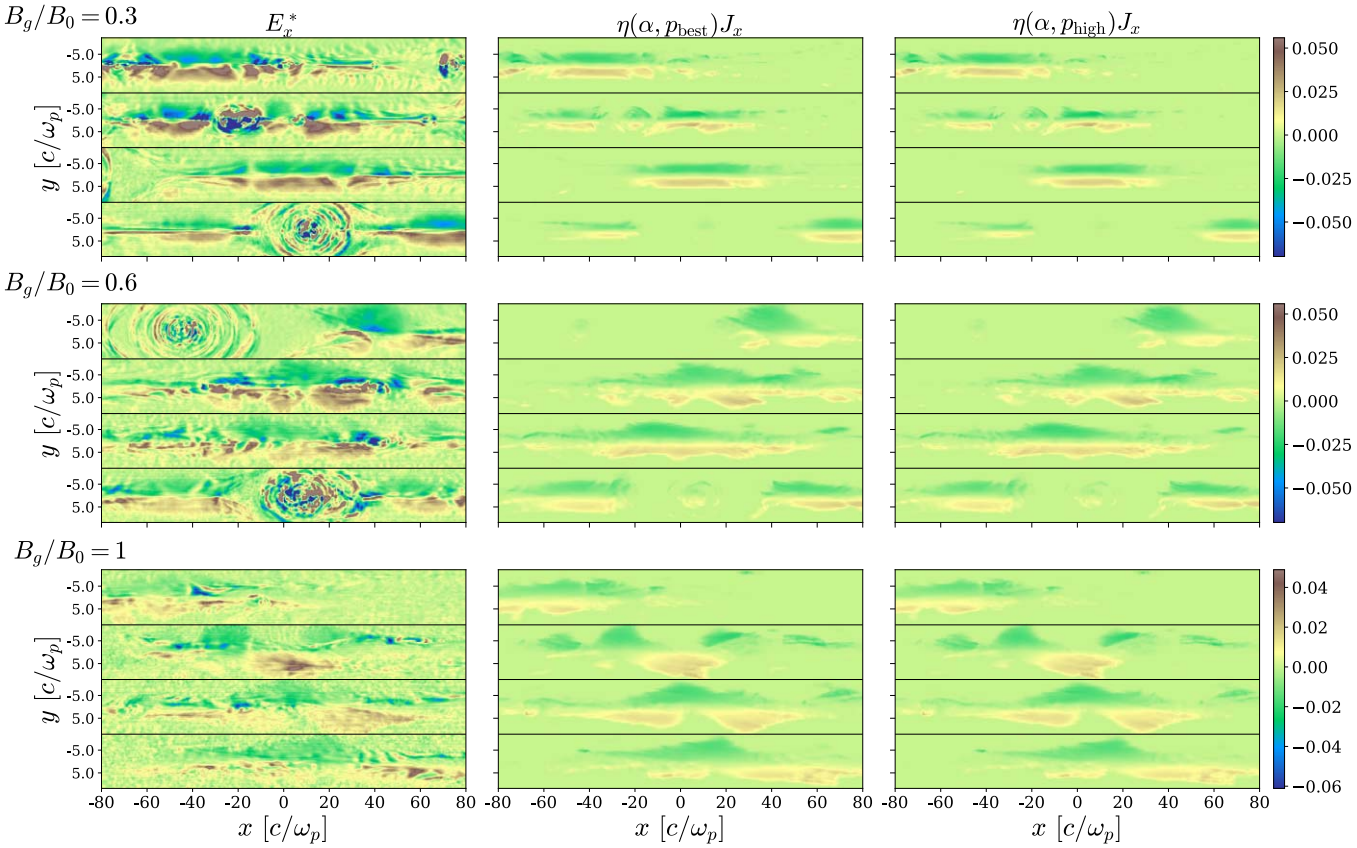

Figure 8. Same as Figure 7, but for the x-component of the nonideal field, which appears for nonzero guide field cases. The resistivity is based on Equation (10) and employs the same values of α and p as in Figure 7. Although our model was not developed using the x-component of $\boldsymbol{E}^*$, it is able to recover the basic structure of regions with significant E_x^*. The magnitude of E_x^* is in units of B_0, and the times shown are the same as in Figure 7.

the value corresponding to $p_{\rm high}$). The plot shows that the two reconstructions are equally good for nonzero guide fields, while for $B_g/B_0 = 0$, the case $\eta_{\rm eff}(\alpha, p_{\rm high})J_z$ seems to capture better the longitudinal extent of nonideal regions. Most importantly, our prescriptive resistivity performs clearly better than the kinetically motivated models presented in Figure 3.

Although our prescriptive resistivity was benchmarked with the z-component of the nonideal field, it can successfully model other nontrivial components that appear for nonzero guide fields. This is shown in Figure 8. While E_y^* is negligible for all guide fields, there are distinct areas in which E_x^* is significant for nonzero guide field cases. We calculate $\eta_{\rm eff}J_x$ via Equation (10) using the same α and p from the analysis of the z-component described above. From the results in Figure 8, we can conclude that the scalar resistivity in Equation (10) provides a satisfactory description of all components of the nonideal electric field across the whole range of guide fields that we explore.

5. Discussion

We have performed a suite of PIC simulations of relativistic pair-plasma reconnection with varying guide field strength, and we have formulated an empirical prescription for the effective resistivity $\eta_{\rm eff}$ in Equation (9) or equivalently Equation (10). Our prescription depends on two free parameters, α and p, which are derived directly from our PIC runs—with $\alpha/2$ expected to be comparable to the dimensionless reconnection rate. As compared to the kinetically motivated model proposed by S. Selvi et al. (2023), the form of $\eta_{\rm eff}$ that we propose has four main advantages: it is explicitly written in single-fluid MHD quantities, does not depend on spatial derivatives, is coordinate agnostic, and is valid for any guide field. It depends only on the electric current density and the particle number density (and the two free parameters discussed above). We have demonstrated that the scalar resistivity we propose successfully describes the spatial structure and strength of all components of the nonideal field. It thus provides a promising strategy for enhancing the reconnection rate in relativistic resistive MHD approaches.

To confirm the robustness of our findings, we demonstrate in Appendix A that the form in Equation (10) (with α and p determined from our reference runs) provides an excellent description of nonideal fields in independent simulations, which either include synchrotron cooling or resolve the plasma skin depth with 20 cells (as compared to 5 cells for our reference runs).

We conclude with an important remark. Our prescription in Equation (9) can be equivalently written as

$$\eta_{\rm eff} = \frac{|\boldsymbol{E}^*|}{en_t c}\left[\frac{\alpha B_0 - |\boldsymbol{E}^*|}{|\boldsymbol{E}^*|}\right]^{\frac{1}{p+1}}. \tag{13}$$

In the limit of very high p, the square bracket is elevated to a very small power, yielding a contribution of order unity. Furthermore, Figure 5 suggests that, as long as p is large, our results do not significantly depend on its precise value. In the

limit $p \gg 1$, the effective resistivity simplifies to

$$\eta_{\rm eff} \simeq \frac{|\boldsymbol{E}^*|}{en_t c}, \tag{14}$$

which has several advantages: it is simple; coordinate agnostic; and no longer depends on the free parameters α and p, i.e., it holds for any guide field strength. It retains the dependence on density that we already emphasized as being of key importance. The approximation $p \gg 1$ holds for all guide fields $B_g/B_0 \geqslant 0.3$; see Figure 6. In Appendix C, we demonstrate that solutions with $p \gg 1$ provide a satisfactory fit also for the case of zero guide field. We therefore regard Equation (14) as the most promising form of effective resistivity to implement in resistive MHD simulations of relativistic reconnection, especially in global problems where it is nontrivial to determine the guide field strength.

We conclude with three caveats. First, our results are based on 2D simulations. While the physics of particle acceleration in relativistic reconnection is dramatically different between 2D and 3D (e.g., H. Zhang et al. 2021, 2023; A. Chernoglazov et al. 2023), the nonideal physics of field dissipation—the focus of our work—is roughly the same (e.g., L. Sironi & A. Spitkovsky 2014; G. R. Werner & D. A. Uzdensky 2017). Yet, dedicated 3D simulations should be performed to confirm our findings. Second, we have employed an electron–positron composition, and future work is needed to confirm our results in the case of electron–proton and electron–positron–proton plasmas. Finally, the generalization of our prescription to the regime of trans- or nonrelativistic reconnection is far from trivial. In fact, the importance of charge starvation and compressibility effects in our prescriptive model, as emphasized in Section 3.2, is likely to change in the case of low magnetization. There, the plasma beta becomes another important parameter governing the reconnection physics. We defer the investigation of the effective resistivity in trans- and nonrelativistic reconnection (for different plasma beta) to future work.

Acknowledgments

We are grateful to Fabio Bacchini, Ashley Bransgrove, Camille Granier, Rony Keppens, Oliver Porth, Sasha Philippov, and Eliot Quataert for useful discussions. L.S. acknowledges support from DoE Early Career Award DE-SC0023015, NASA ATP 80NSSC24K1238, NASA ATP 80NSSC24K1826, and NSF AST-2307202. This work was supported by a grant from the Simons Foundation (MP-SCMPS-00001470) to L.S. and B. R. and facilitated by the Multimessenger Plasma Physics Center (MPPC), grant PHY-2206609 to L.S. and S.S. B.R. and A.L. are supported by the Natural Sciences & Engineering Research Council of Canada (NSERC). B.R. is supported by the Canadian Space Agency (23JWGO2A01). B.R. acknowledges a guest researcher position at the Flatiron Institute, supported by the Simons Foundation. E.R.M. acknowledges support by the National Science Foundation under grants No. PHY-2309210 and AST-2307394 and from NASA's ATP program under grant 80NSSC24K1229. The computational resources and services used in this work were partially provided by Columbia University (Ginsburg HPC cluster) and by facilities supported by the Scientific Computing Core at the Flatiron Institute, a division of the Simons Foundation.

Appendix A
Additional Validations

We validate our results on two additional sets of simulations having zero guide field: first, we increase the spatial resolution, and then we perform simulations with strong synchrotron cooling. In all the cases, we find that our prescription in Equation (10)—using the same α and p as determined in the main text (see Table 2)—provides a successful reconstruction of the nonideal field.

We first confirm our findings with a higher-resolution simulation ($c/\omega_p = 20$ cells) having zero guide field. The length of the domain in the x-direction is $L_x = 480\, c/\omega_p$. The results in Figure 9 confirm the robustness of our conclusions, with $\eta_{\rm eff}(\alpha, p_{\rm high})J_z$ visually providing the best proxy for the nonideal field.

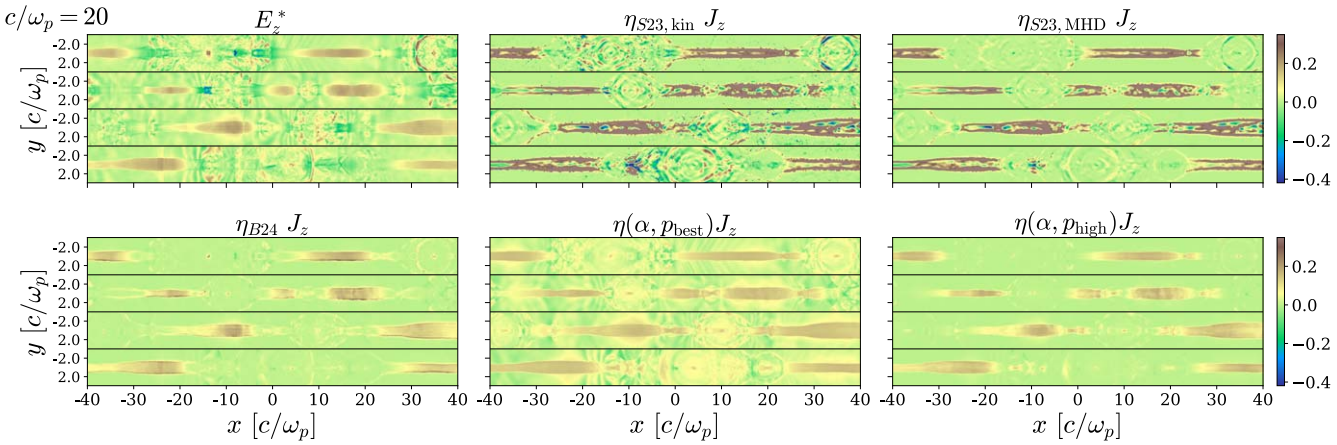

Figure 9. A comparison of the measured E_z^* and various reconstructions $\eta_{\rm eff}J_z$ using different forms of the resistivity. Top row, from left to right: ground truth, Equation (3), and Equation (5). Bottom row, from left to right: Equation (7) and Equation (10) for both $p_{\rm best}$ and $p_{\rm high}$ (and their respective best-fit α values, calculated from the functions in Table 2). The simulation has zero guide field and a spatial resolution of $c/\omega_p = 20$ cells. All panels are normalized to B_0. Within each panel, horizontal black lines separate different time snapshots: at the start of the quasi-steady phase and after 112.5, 202.5, and 270 ω_p^{-1}.

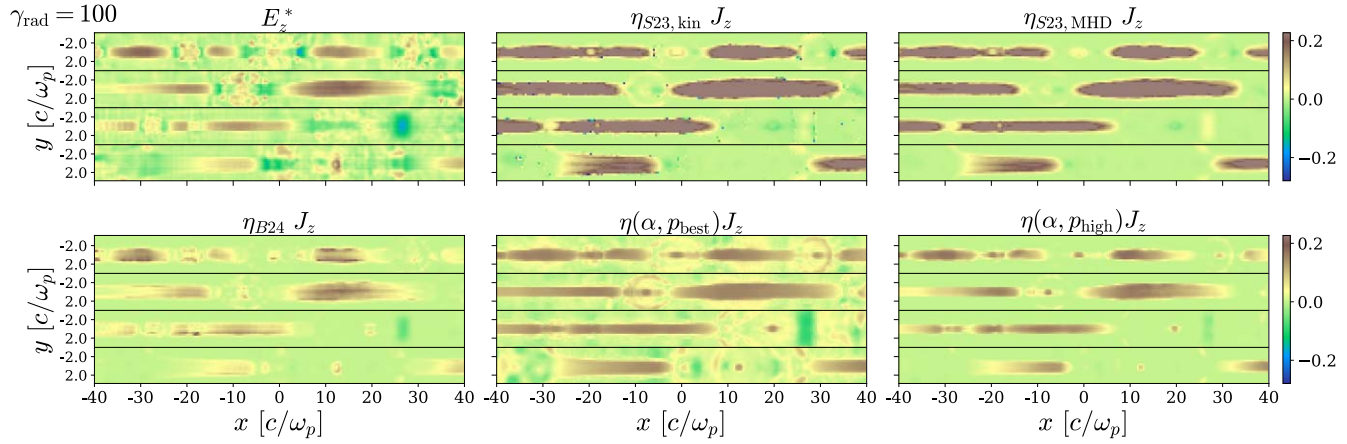

Figure 10. Same as Figure 9 but for standard resolution ($c/\omega_p = 5$ cells) and with the addition of synchrotron cooling losses, as quantified by $\gamma_{\rm rad} = 100$ (weak cooling regime, since $\gamma_{\rm rad} > \sigma$). Within each panel, horizontal black lines separate different time snapshots: at the start of the quasi-steady phase and after 450, 810, and 1080 ω_p^{-1}.

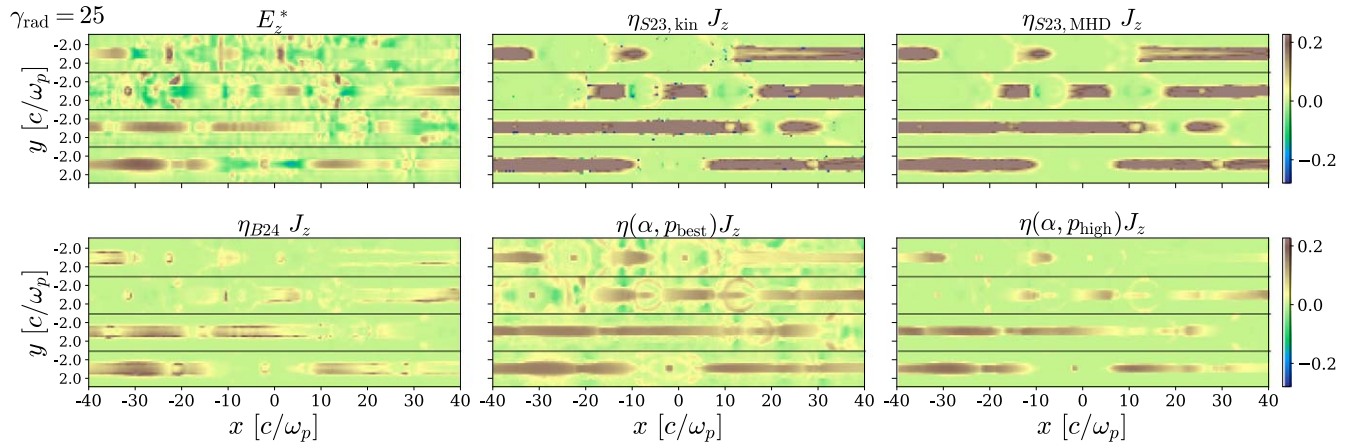

Figure 11. Same as Figure 9 but for standard resolution ($c/\omega_p = 5$ cells) and with the addition of synchrotron cooling losses, as quantified by $\gamma_{\rm rad} = 25$ (strong cooling regime, since $\gamma_{\rm rad} < \sigma$). We show the same time snapshots as in Figure 10.

We also perform simulations with synchrotron cooling losses and the fiducial resolution of $c/\omega_p = 5$ cells. We quantify the cooling strength via the radiation-reaction Lorentz factor $\gamma_{\rm rad}$, also known as the classical "burn-off" limit, at which the radiation-reaction drag force balances the accelerating force of the reconnection electric field, yielding

$$\gamma_{\rm rad} = \sqrt{\frac{e(v_{in}/c)B_0}{(4/3)\sigma_{\rm T}(B_0^2/8\pi)}}. \tag{A1}$$

The results in Figures 10 and 11 confirm the robustness of our conclusions, both for weak ($\gamma_{\rm rad} = 100$) and strong ($\gamma_{\rm rad} = 25$) cooling. In particular, our prescription $\eta_{\rm eff}(\alpha, p_{\rm high})J_z$ visually appears to provide the best proxy for the nonideal field. In summary, Equation (10)—with α and p determined from the fiducial simulations discussed in the main text—can be successfully applied to other runs, including the important case of strong cooling losses.

Appendix B
The Full Ohm's Law

In the main text, we reduced the full Ohm's law for resistive relativistic single-fluid MHD (Equation (1)) to the simpler form in Equation (2). We verify in Figure 12 that our results still hold when using the full relativistic Ohm's law for resistive MHD, as given in Equation (1). Differences with respect to Figure 7 are minor, especially in lower guide field cases. For simulations with stronger guide fields, we see that when the full Ohm's law is used, the agreement between our model and the ground truth in plasmoid cores improves.

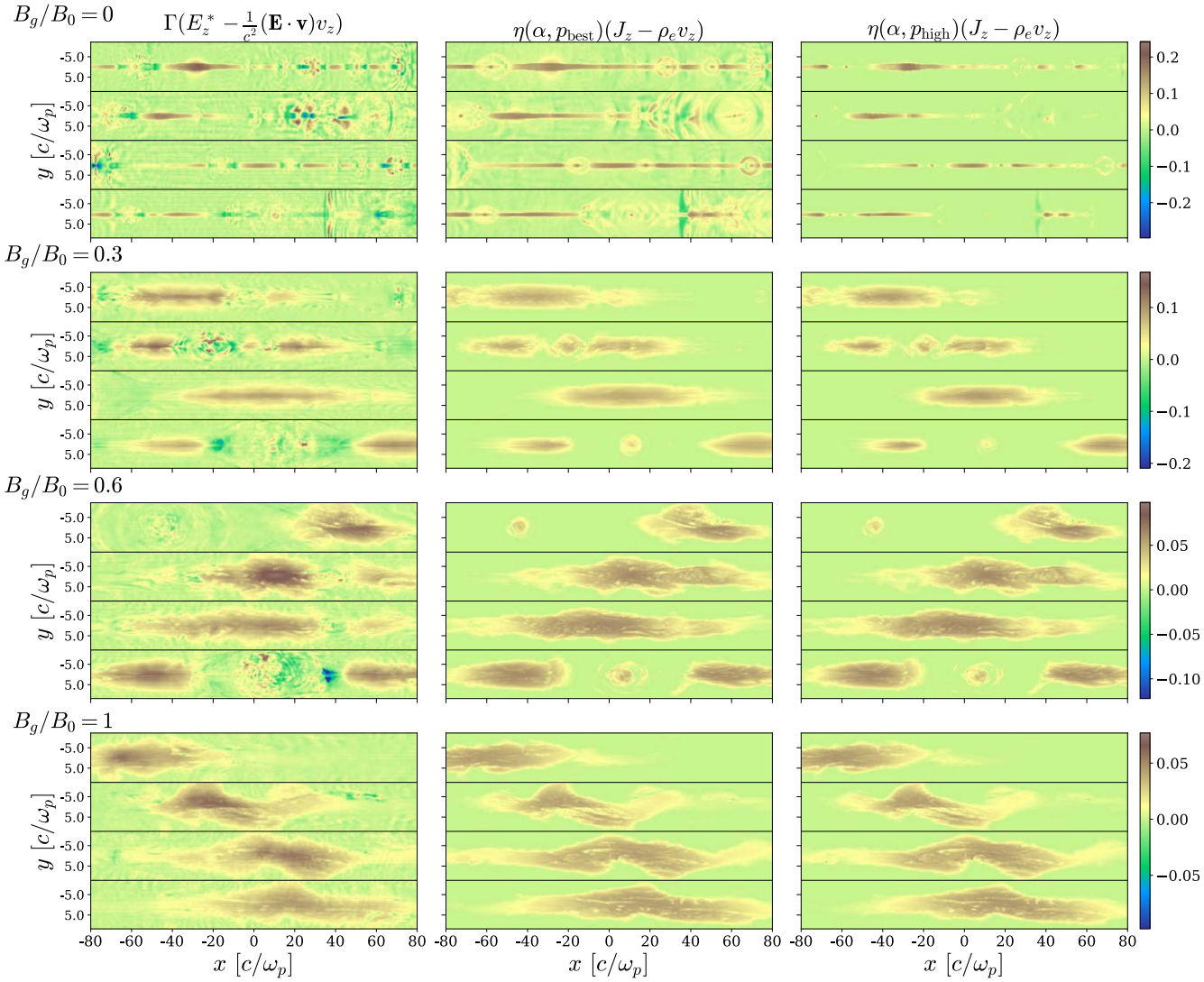

Figure 12. Same as Figure 7 but including all terms in the Ohm's law for resistive relativistic single-fluid MHD (Equation (1)) instead of the simplified form in Equation (2), which we used in the main paper. We still employ our prescription (Equation (10)) with the same α and p as discussed in the main text.

Appendix C
Extending the Range of p for Zero Guide Field

In Figure 7, we have shown that higher values of p appear to reconstruct more accurately the nonideal electric fields in the case of zero guide field, despite yielding formally higher loss values. Motivated by this, we explore how the 2D spatial structure of $\eta_{\rm eff} J_z$, with $\eta_{\rm eff}$ in Equation (10), changes when using values of p higher than $p_{\rm high}$ (for each p, we use the α value given by the function in Table 2). The results shown in Figure 13 show that values of p greater than $p_{\rm high}$ up to at least $p = 4$ provide an excellent reconstruction of the ground truth.

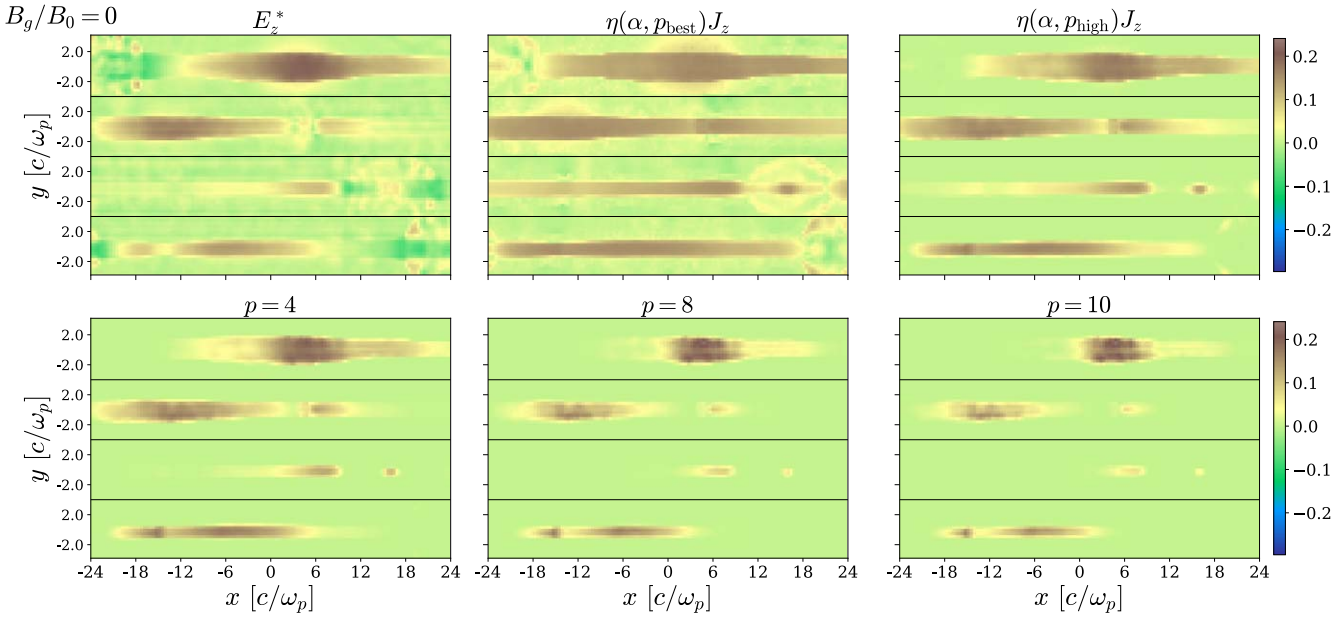

Figure 13. A comparison of the measured E_z^* and the reconstruction $\eta_{\rm eff}J_z$ using Equation (10). We vary p beyond the range given in Table 1, and for each p, we use the optimal α value calculated from the functions presented in Table 2. The simulation has zero guide field, no cooling, and a spatial resolution of $c/\omega_p = 5$ cells (i.e., it is the reference run used in the main paper). All panels are normalized to B_0. The time snapshots are the same as in Figures 3 and 7.

ORCID iDs

Abigail Moran https://orcid.org/0000-0002-6437-5229
Lorenzo Sironi https://orcid.org/0000-0002-1227-2754
Aviad Levis https://orcid.org/0000-0001-7307-632X
Bart Ripperda https://orcid.org/0000-0002-7301-3908
Elias R. Most https://orcid.org/0000-0002-0491-1210
Sebastiaan Selvi https://orcid.org/0000-0001-9508-1234

References

Alfvén, H. 1943, ArMAF, 29B, 1
Bessho, N., & Bhattacharjee, A. 2005, PhRvL, 95, 245001
Bessho, N., & Bhattacharjee, A. 2007, PhPl, 14, 056503
Bessho, N., & Bhattacharjee, A. 2010, PhPl, 17, 102104
Bessho, N., & Bhattacharjee, A. 2012, ApJ, 750, 129
Birn, J., Drake, J. F., Shay, M. A., et al. 2001, JGR, 106, 3715
Biskamp, D., & Schwarz, E. 2001, PhPl, 8, 3282
Bransgrove, A., Ripperda, B., & Philippov, A. 2021, PhRvL, 127, 055101
Bugli, M., Lopresti, E. F., Figueiredo, E., et al. 2024, arXiv:2410.20924
Cai, H. J., & Lee, L. C. 1997, PhPl, 4, 509
Cassak, P. A., Liu, Y. H., & Shay, M. A. 2017, JPlPh, 83, 715830501
Chernoglazov, A., Hakobyan, H., & Philippov, A. 2023, ApJ, 959, 122
Comisso, L., & Bhattacharjee, A. 2016, JPlPh, 82, 595820601
Del Zanna, L., Zanotti, O., Bucciantini, N., & Londrillo, P. 2007, A&A, 473, 11
Egedal, J., Ng, J., Le, A., et al. 2019, PhRvL, 123, 225101
Galishnikova, A., Philippov, A., Quataert, E., et al. 2023, PhRvL, 130, 115201
Goodbred, M., & Liu, Y.-H. 2022, PhRvL, 129, 265101
Guo, F., Liu, Y.-H., Li, X., et al. 2020, PhPl, 27, 080501
Guo, F., Liu, Y.-H., Zenitani, S., & Hoshino, M. 2024, SSRv, 220, 43
Harris, E. G. 1962, NCim, 23, 115
Hesse, M., & Zenitani, S. 2007, PhPl, 14, 112102
Hirvijoki, E., Lingam, M., Pfefferlé, D., et al. 2016, PhPl, 23, 080701
Horiuchi, R., & Sato, T. 1994, PhPl, 1, 3587
Hoshino, M., & Lyubarsky, Y. 2012, SSRv, 173, 521
Kagan, D., Sironi, L., Cerutti, B., & Giannios, D. 2015, SSRv, 191, 545
Komissarov, S. S. 2007, MNRAS, 382, 995
Kulsrud, R. M. 1998, PhPl, 5, 1599
Kulsrud, R. M. 2001, EP&S, 53, 417
Kuznetsova, M. M., Hesse, M., & Winske, D. 1998, JGR, 103, 199
Lingam, M., Hirvijoki, E., Pfefferlé, D., Comisso, L., & Bhattacharjee, A. 2017, PhPl, 24, 042120
Loureiro, N. F. 2023, arXiv:2312.06945
Lyons, L. R., & Pridmore-Brown, D. C. 1990, JGR, 95, 20903
Melzani, M., Walder, R., Folini, D., Winisdoerffer, C., & Favre, J. M. 2014, A&A, 570, A111
Ripperda, B., Porth, O., Sironi, L., & Keppens, R. 2019, MNRAS, 485, 299
Selvi, S., Porth, O., Ripperda, B., et al. 2023, ApJ, 950, 169
Sironi, L. 2022, PhRvL, 128, 145102
Sironi, L., & Spitkovsky, A. 2014, ApJL, 783, L21
Spitkovsky, A. 2005, in AIP Conf. Ser. 801, Astrophysical Sources of High Energy Particles and Radiation, ed. T. Bulik, B. Rudak, & G. Madejski (Melville, NY: AIP), 345
Totorica, S. R., Zenitani, S., Matsukiyo, S., et al. 2023, ApJL, 952, L1
Uzdensky, D. 2003, APS Division of Plasma Physics Meeting, 45, BO2.003
Uzdensky, D. A., Loureiro, N. F., & Schekochihin, A. A. 2010, PhRvL, 105, 235002
Werner, G. R., & Uzdensky, D. A. 2017, ApJL, 843, L27
Zenitani, S., Hesse, M., & Klimas, A. 2010, ApJL, 716, L214
Zhang, H., Sironi, L., & Giannios, D. 2021, ApJ, 922, 261
Zhang, H., Sironi, L., Giannios, D., & Petropoulou, M. 2023, ApJL, 956, L36